Evaluation of coarse-grained CFD-DEM models with the validation of PEPT measurements

Che, Hanqiao; Werner, Dominik; Seville, Jonathan; Wheldon, Tzany Kokalova; Windows-Yule, Kit

DOI:
10.1016/j.partic.2022.12.018

Document Version
Publisher's PDF, also known as Version of record

Citation for published version (Harvard):
Che, H, Werner, D, Seville, J, Wheldon, TK & Windows-Yule, K 2023, 'Evaluation of coarse-grained CFD-DEM models with the validation of PEPT measurements', *Particuology*, vol. 82, pp. 48-63. https://doi.org/10.1016/j.partic.2022.12.018

Particuology 82 (2023) 48–63

Contents lists available at ScienceDirect

Particuology

journal homepage: www.elsevier.com/locate/partic

Evaluation of coarse-grained CFD-DEM models with the validation of PEPT measurements

Hanqiao Che [a], Dominik Werner [a], Jonathan Seville [a], Tzany Kokalova Wheldon [b], Kit Windows-Yule [a,*]

[a] School of Chemical Engineering, University of Birmingham, B15 2TT, UK
[b] School of Physics and Astronomy, University of Birmingham, Birmingham, B15 2TT, UK

ARTICLE INFO

Article history:
Received 9 September 2022
Received in revised form
16 November 2022
Accepted 21 December 2022
Available online 20 January 2023

Keywords:
Coarse-graining
Discrete element method
Computational fluid dynamics
CFD-DEM
Positron emission particle tracking (PEPT)
Bubbling fluidised bed

ABSTRACT

Computational Fluid Dynamics coupled with Discrete Element Method (CFD-DEM) is a commonly used numerical method to model gas-solid flow in fluidised beds and other multiphase systems. A significant limitation of CFD-DEM is the feasibility of the realistic simulation of large numbers of particles. Coarse-graining (CG) approaches, through which groups of multiple individual particles are represented by single, larger particles, can substantially reduce the total number of particles while maintaining similar system dynamics. As these three CG models have not previously been compared, there remains some debate, however, about the best practice in the application of CG in CFD-DEM simulations. In this paper, we evaluate the performance of three typical CG methods based on simulations of a bubbling fluidised bed. This is achieved through the use of a numerical validation framework, which makes full use of the high-resolution 3D positron emission particle tracking (PEPT) measurements to rigorously validate the outputs of CFD-DEM simulations conducted using various different coarse-graining models, and various different degrees of coarse-graining. The particle flow behaviours in terms of the particle occupancy field, velocity field, circulation time, and bubble size and velocity, are comprehensively analysed. It is shown that the CG simulation starts to fail when the size ratio between the bed chamber and the particles decreases to approximately 20. It is also observed, somewhat surprisingly, that the specific CG approach applied to interparticle contact parameters does not have a substantial effect on the simulation results for the bubbling bed simulations across a wide range of CG factors.

1. Introduction

Fluidised beds are widely applied in many industrial areas, such as chemical reactions (Werther, Hartge, & Heinrich, 2014), the coating or drying of pharmaceutical granules (Toschkoff & Khinast, 2013), or the treatment of biomass and waste (Hofbauer & Materazzi, 2019; Iannello, Foscolo, & Materazzi, 2021). Understanding the gas-solid flow behaviour in a bubbling fluidised bed is essential for the optimization and design of these, and myriad other, processes. CFD-DEM is a numerical method to model such processes. In typical CFD-DEM simulations of fluidised beds, the fluidization air is treated as an incompressible fluid. The void fraction, which is defined as the void ratio of a CFD mesh cell, is introduced to account for the presence of the particle phase in the Navier-Stokes equations (Zhou, Kuang, Chu, & Yu, 2010), while the motion of the particulate phase is solved by the discrete element method (DEM). Therefore, CFD-DEM provides information with particle-scale resolution, requires comparatively fewer assumptions, and is thus capable of providing more precise solutions than two fluid model (TFM) and multiphase particle-in-cell (MP-PIC) simulations (Moliner et al., 2019).

A drawback of CFD-DEM is the feasibility of realistic simulations possessing large numbers of particles (Di Renzo, Napolitano, & Di Maio, 2021), as typically required for industrial applications. Representing all particles in a full-scale fluidised bed is not possible owing to the current limitation of computational resource. This issue can, however be addressed – to an extent - by reducing the total particle number in the simulation through the application of coarse-graining methods.

* Corresponding author.
E-mail address: c.r.windows-yule@bham.ac.uk (K. Windows-Yule).

https://doi.org/10.1016/j.partic.2022.12.018

Nomenclature

A	Area, m^2
Co	Courant number,
d	Diameter, m
$\mathbf{F}_d$	Drag force, N
$\mathbf{F}_{\nabla p}$	Pressure gradient force, N
$\mathbf{F}_{\nabla \bullet \tau}$	Viscous force induced by the air, N
$\mathbf{g}$	Gravitational acceleration, m/s^2
G	Shear modulus, GPa
G_{pf}	Particle-fluid momentum source coefficient, $kg/(m^3 s)$
$\mathbf{I}$	Moment of inertia, kg m^2
k	Elastic constant, GPa
m	Mass, kg
N	Number of particles,
p	Air pressure, Pa
R	Radius of a particle, m
t	Time, s
$\mathbf{u}$	Velocity, m/s
C_i	Constant term in an equation for CG

Greek symbols

γ	Viscoelastic damping constant, 1/(m s)
θ	Size ratio between diameter of particle and fluidised bed,
ε	Void fraction,
λ	CG factor,
μ	Dynamic viscosity, Pa s
ν	Kinematic viscosity, m^2/s
ρ	Density, kg/m^3
$\boldsymbol{\tau}$	Viscous force tensor, Pa
$\boldsymbol{\omega}$	Angular velocity, 1/s

Subscripts

b	Bubble
eff	Effective
f	Fluid
fl	Fluidization
p	Particle

As reviewed by Alberto et al. (Di Renzo et al., 2021), the CG rules relating to particle contact interactions can vary according to different conceptions of the "similarity" of particle interactions. Considering the linear spring-dashpot-slider contact force model, two CG strategies, namely constant absolute overlap models (which conserve the typical energy contents of the particle/grain system before and after the collisions) (Sakai et al., 2010, 2014; Sakai & Koshizuka, 2009; Takabatake, Mori, Khinast, & Sakai, 2018), and constant relative overlap models (Radl, Radeke, Khinast, & Sundaresan, 2011), have been applied. The constant absolute overlap method is intended to be able to keep dissipated energy during collisions constant (Sakai & Koshizuka, 2009). Many research works have also been performed by applying CG methods which totally ignore the coarse graining of particle contact forces (Heinrich, Dosta, & Antonyuk, 2015; Link, Cuypers, Deen, & Kuipers, 2005). This conception is reasonable for two reasons: Firstly, the fluid-particle interaction force is expected to play the dominant role in the gas-solid flow in a fluidised bed; second, it is difficult to define a meaningful mapping between the contact force felt by a coarse-grained pseudo-particle and the forces experienced by the group of individual particles it is meant to represent, as these "real" particles will be free to move in different directions, while the "virtual" CG particle can clearly only travel in one direction at a time (Liu, Suda, Tsuji, & Tanaka, 2013). It should be noted that the inter-particle contact parameters may not be critical for the fluidised bed simulations as even very simplified models like hard sphere DEM still provide fairly good results (Link et al., 2009; Liu et al., 2013). As is clear from the above, there exists significant debate in the literature regarding the best way to implement CG in CFD-DEM simulations, and even if it is necessary to apply CG rules to the particle contact forces in the case of drag-dominated systems such as dilute fluidised beds.

Though CFD-DEM has been widely applied in simulations of fluidised beds at various different scales (Zhu, Zhou, Yang, & Yu, 2008), previous CFD-DEM simulations rarely got an opportunity to be validated rigorously, especially through the application of techniques offering particle-scale resolution. The reason for this is that most existing experimental approaches cannot provide precise information regarding individual particle motion within realistic, three-dimensional fluidised beds. For example, pressure drop measurements (da Silva, Butzge, Nitz, & Taranto, 2014; van Ommen et al., 2011) mainly carry the information related to macroscopic flow properties rather than the velocity or solid distributions; optical approaches such as a high-speed camera (Breuninger et al., 2018; Link et al., 2005), particle image velocimetry (PIV) (Annaland, Herguido, & Menéndez, 2012; Gryczka et al., 2008; Julián et al., 2012; Westerweel, Elsinga, & Adrian, 2013) can provide only a limited, quasi-two-dimensional field of view, and cannot visualise the interior dynamics of opaque systems; electrical capacitance tomography (ECT) (Che et al., 2020; Che, Ye, Tu, Yang, & Wang, 2018; Wang & Yang, 2020) can only offer the solid concentration information with a relatively low resolution, and is unsuitable for imaging metal-walled systems as are often found in industry. Though particle motion *can* be tracked using particle tracking velocimetry (PTV) (Hagemeier, Roloff, Bück, & Tsotsas, 2015) or magnetic particle tracking (MPT) (Buist, van der Gaag, Deen, & Kuipers, 2014; Grohn, Oesau, Heinrich, & Antonyuk, 2022; Mohs, Gryczka, Heinrich, & Mörl, 2009; Neuwirth, Antonyuk, Heinrich, & Jacob, 2013; Oesau, Grohn, Pietsch-Braune, Antonyuk, & Heinrich, 2022), the former is only suitable for highly-dilute and/or quasi-two-dimensional systems, while the latter requires the use of tracers significantly larger than those used in most real, industrial systems (C. R. Windows-Yule et al., 2021; Rosato, A. D., & Windows-Yule, C. (2020)). The development of Positron Emission Particle Tracking provided the opportunity to overcome such limitations. Positron emission particle tracking (PEPT) is a technique which facilitates the high temporal and spatial resolution tracking of radioactively labelled tracer particles moving in particulate or multiphase systems (C. Windows-Yule, Seville, Ingram, & Parker, 2020; C. R. Windows-Yule et al., 2021; K. Windows-Yule, Nicuşan, Herald, Manger, & Parker, 2022). In order to perform PEPT, a radioisotope (here Fluorine-18) is incorporated into a tracer particle which undergoes beta decay involving emission of a positron. The radioactively labelled tracer particle, which is physically identical to all others in the system (making PEPT truly non-invasive) is placed in the mixture. Based on the measurement of the gamma photons, when two γ photons produced by an annihilation event are detected, their trajectory can be reconstructed to give a single line of response (LoR). With a suitably large number of LoRs, the location of the individual particle can be determined accurately and frequently as it moves within a piece of equipment (see Fig. 1). By exploiting the principle of ergodicity (Wildman, Huntley, Hansen,

Parker, & Allen, 2000), this Lagrangian information can be used to create detailed, three-dimensional Eulerian fields, such as velocity (vector) fields and solid fraction (occupancy) distributions, amongst diverse others (C. Windows-Yule, Gibson, et al., 2020). PEPT has been widely used in the imaging of diverse fluidised- and spouted-bed systems (Al-Shemmeri, Windows-Yule, Lopez-Quiroga, & Fryer, 2021; Hoomans, Kuipers, Mohd Salleh, Stein, & Seville, 2001; Laverman et al., 2012; Seiler, Fryer, & Seville, 2008; Stein, Ding, Seville, & Parker, 2000; Stein, Martin, Seville, McNeil, & Parker, 1997; Tebianian et al., 2015; Van de Velden, Baeyens, Seville, & Fan, 2008; C. R. K. Windows-Yule, A. Moore et al., 2020; C. R. K. Windows-Yule, S. Gibson et al., 2020; Wong & Seville, 2006; Xu et al., 2020; Che et al., 2023).

With the help of the high temporal and spatial resolution of PEPT measurements in a simple bubbling fluidised bed, the objective of this paper is to evaluate the performance of CFD-DEM coarse-graining methods, and the range of coarse-graining (scale-up) factors across which they can be successfully applied. This paper is organized as follows: In section 2 and 3, respectively, the experimental conditions used for PEPT measurements and the CFD-DEM CG model are briefly introduced; in section 4, the post-processing procedures which allow a direct comparison of the numerical and experimental results are introduced; following a detailed comparison (and validation) of the CG methods in section 5, conclusions are drawn in section 6.

2. PEPT experiment

Several PEPT experiments were performed using silica sand with a mean diameter of 357 μm and a density of 2700 kg/ m^3 and a cylindrical fluidised bed with an inner diameter of 9.4 cm. Fig. 2 shows the particle diameter distribution of the sand, and Fig. 3 shows the dimensions of the fluidised bed and the air distributor. The full particle properties of the various samples used are shown in Table 1. The minimum fluidization air velocity (u_{mf}) was measured in experiments, in which u_{fl} was increased slowly and curve of u_{fl} versus pressure drop was plotted. u_{mf} is equal to the u_{fl} at the turning point of the pressure drop curve. The air velocities are set to 2–3 u_{mf}. The bubbling bed was placed between the two detector heads of a modified ADAC Forte positron camera (Parker, Forster, Fowles, & Takhar, 2002; C. Windows-Yule, Gibson, et al., 2020). The Forte camera system at the University of Birmingham has the capability to locate a tracer travelling at 1 m/s to within 0.5 mm approximately 250 times a second. The PEPT-ML algorithm (Nicuşan & Windows-Yule, 2020) was used to locate and track the particle. Data were captured over 2 h, a duration sufficient for the tracer particle to fully explore the fluidised bed.

The data output from the experiments is a sequence of locations in the form (t, x, y, z) representing the path of the tracer. These

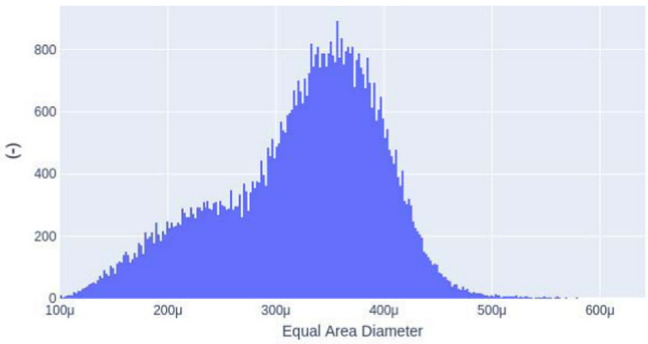

Fig. 2. Particle diameter distribution.

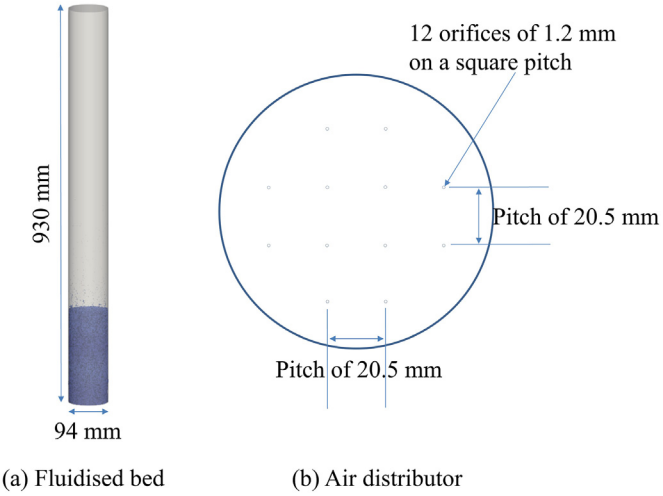

Fig. 3. Dimensions of the fluidised bed and the air distributor.

Table 1
Properties of sand particles used in the experiments.

Parameters	Unit	Value
Density	kg/m^3	2700
Total mass	kg	2.08
Mean diameter	μm	357
Sphericity	–	0.95
Shear modulus, G	GPa	0.005
Poisson's ratio, ν	–	0.25
Restitution coefficient, e	–	0.6
Frictional coefficient, f	–	0.3

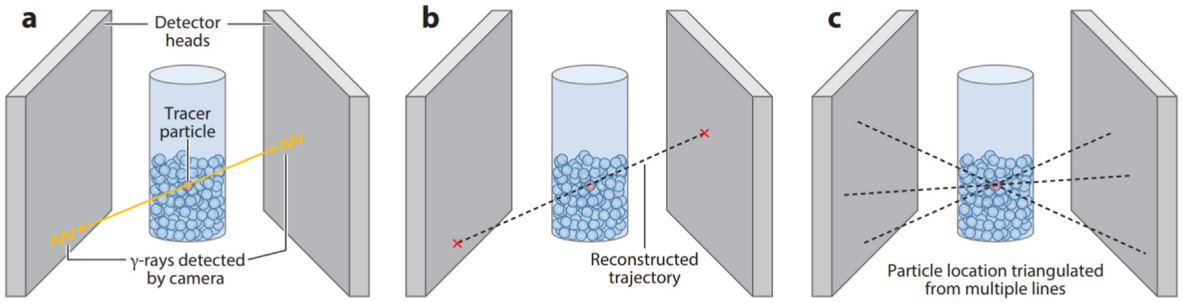

Fig. 1. How positron emission particle tracking (PEPT) locates a single tracer particle in a granular system (Cited from (C. R. Windows-Yule et al., 2021)). (a) A pair of gamma rays emitted by the radioactively-labelled tracer particle are detected by a suitable gamma camera. (b) The straight-line path followed by the annihilation pair is algorithmically reconstructed. (c) The intersection point of multiple such "lines of response" can be used to triangulate the pseudo-instantaneous position of the tracer.

locations can then be used to extract useful information such as time-averaged velocity field and fractional occupancy field, which will be introduced in the following section.

3. Coarse-grained CFD-DEM

3.1. Governing equations

The governing equations of both fluid and particle motion are shown in Table 2. The "divided" void fraction model, which distributes the particle volume to the CFD mesh cells, is applied (Kloss, Goniva, Hager, Amberger, & Pirker, 2012). In order to simplify the CG process of inter-particle contact force, the linear spring-dashpot-slider model (Cundall & Strack, 1979; Di Renzo & Di Maio, 2004) is used. Despite its simplicity, this model has been repeatedly shown to be suitable for the simulation of fluidised beds (Mori, Wu, & Sakai, 2019; Mu, Buist, Kuipers, & Deen, 2020; Zhu, Zhou, Yang, & Yu, 2007). Its simplicity also carries the significant benefit of increasing the computational efficiency of our simulations compared to other, more complex models. More details about CFD-DEM calculation can be found in (Zhou et al., 2010).

The governing equations of the two phases are solved sequentially in CFD-DEM calculations; the information related to the particle-fluid interaction force, particle velocity and void fraction are exchanged between the solvers at each coupling interval.

3.2. Coarse-grain methods

As there is some debate in the literature on the best way to implement CG in CFD-DEM simulations, here we compare several representative CG methods: dimensionless number model, constant absolute overlap model and constant relative overlap model. As the details of each of these models are contained in previous publications (Bierwisch, Kraft, Riedel, & Moseler, 2009; Di Renzo et al., 2021; Link et al., 2009; Mori et al., 2019; Mu et al., 2020), we only give a general description in Appendix A.

Table 3 shows the rules of the three CG models (A, B and C represent the models based on constant absolute overlap (Mu et al., 2020), constant relative overlap (Mori et al., 2019), and dimensionless number (Link et al., 2009), see Appendix A for more details) under the CG factor of λ, the definition of the variables can be found in the nomenclature. As highlighted above, the contact parameters (k_n, k_t, γ_n, γ_t) are unchanged for the CG method C; thus the CG parameters for those contact parameters are kept to 1. From Table 3, the CG laws related to the fluid-particle interaction force are generally equivalent (apart from those properties related to the particle contact) even though they are derived from different principles. The differences mainly lie in the treatment of the inter-particle contact force terms.

As for the CG of polydisperse particle systems, there are two main strategies (Di Renzo et al., 2021; Lu, Xu, Li, & Benyahia, 2018), i.e., same statistical weight (SSW) and same size parcel (SSP). SSW method maintains a PSD identical to that of the original powder, while the SSP method uses different statistical weights for particles with different diameters and scales the original polydisperse powder to a coarse mono-disperse powder with same size parcel (Lu et al., 2018). Here we adopt the SSW method, as it maintains the polydisperse particles in the simulation and showed better performance than SSP at low Reynolds number (Lu et al., 2018).

Table 2
Governing equations applied in the CFD-DEM model.

Governing equations for fluid phase

Continuity equations:

$$\frac{\partial}{\partial t}(\varepsilon\rho_f) + \nabla \bullet (\varepsilon\rho_f \mathbf{u}_f) = 0$$

Momentum equations:

$$\frac{\partial}{\partial t}(\varepsilon\rho_f \mathbf{u}_f) + \nabla \bullet (\varepsilon\rho_f \mathbf{u}_f \otimes \mathbf{u}_f) = -\varepsilon\nabla p + \varepsilon\nabla \bullet \boldsymbol{\tau}_f - (G_{pf}\mathbf{u}_f - G_{pf}\langle \mathbf{u}_p \rangle) + \varepsilon\rho_f \mathbf{g}$$

$$G_{pf} = \frac{|\sum_i \mathbf{F}_{d,i}|}{V_{cell}|\mathbf{u}_f - \langle \mathbf{u}_p \rangle|}$$

Ergun-Wen & Yu drag force model (Ergun, 1952; Wen & Yu, 1966):

$$\mathbf{F}_d = \begin{cases} \dfrac{V_p \eta_f}{\psi_p^2 d_p^2}\left[150\dfrac{1-\varepsilon}{\varepsilon} + 1.75\dfrac{\mathrm{Re}}{\varepsilon}\right](\mathbf{u}_f - \mathbf{u}_p), \varepsilon \le 0.8 \\ 0.75\dfrac{24 V_p \eta_f}{\psi_p^2 d_p^2 \varepsilon^{2.65}}(1 + 0.15\mathrm{Re}^{0.687})(\mathbf{u}_f - \mathbf{u}_p), \varepsilon > 0.8 \end{cases}$$

Governing equations for solid phase $m_{p,i}\dfrac{\mathrm{d}\mathbf{u}_{p,i}}{\mathrm{d}t} = \sum_{j=1}^{N_{pj}} \mathbf{F}_{c,ij} + \mathbf{F}_{pf,i} + m_{p,i}\mathbf{g}$

$$\mathbf{I}_i \frac{\mathrm{d}\omega_i}{\mathrm{d}t} = \mathbf{T}_i$$

$$\mathbf{F}_{c,ij} = (k_n \delta_{ij} \mathbf{n}_{ij} - \gamma_n \mathbf{u}_{p,n,ij}) + (k_t \Delta \mathbf{s}_{t,ij} - \gamma_t \mathbf{u}_{p,t,ij}),\ |\mathbf{F}_{t,ij}| \le X_\mu |\mathbf{F}_{n,ij}|$$

$$\mathbf{F}_{pf,i} = \mathbf{F}_{d,i} + \mathbf{F}_{\nabla p,i} + \mathbf{F}_{\tau,i}$$

Table 3
CG coefficients in different CG methods[a].

Input parameters	CG methods		
	A	B	C
N_p	$\frac{1}{\lambda^3}$	$\frac{1}{\lambda^3}$	$\frac{1}{\lambda^3}$
μ_g	λ	λ	λ
d_p	λ	λ	λ
ρ_p	$\frac{1}{\lambda}$	$\frac{1}{\lambda}$	$\frac{\rho_{p,1}-\rho_{g,1}}{\lambda\rho_{p,1}} + \frac{\rho_{g,2}}{\rho_{p,1}}$
k_n	λ	λ^2	1
k_t	λ	λ^2	1
γ_n	λ^2	λ^2	1
γ_t	λ^2	λ^2	1

[a] As the density of solid was also adjusted in the three CG methods in this work, the CG parameters for the k_n, k_t, γ_n, γ_t are different from the values given in the reference (Di Renzo et al., 2021).

3.3. Simulation setup

The coarse-grained CFD-DEM models were implemented in a modified version of the open-source code CFDEM (Goniva, Kloss, Hager, & Pirker, 2010; Kloss et al., 2012), which couples two other open-source software packages, the CFD solver OpenFOAM (Weller, Tabor, Jasak, & Fureby, 1998) and the DEM solver LIGGGHTS (Kloss et al., 2012). As Table 4 shows, six simulation cases with different CG factors were set; the input parameters were determined according to the operational conditions in the experiments introduced in the section above; CFD meshes were generated to ensure the cell side length greater than the particle diameter after the CG, the supporting rationale for this setting will be shown in section 5.1. The total physical time in the simulation was 12 s. In order to compare the performance of different CG methods, three different simulations were performed for each case using methods A, B and C, respectively. It should be noted that the air velocities (2–3 u_{mf}) applied in the simulations are suitable for the CG method validation as the contacts/multiparticle contacts are longer-lasting than in the case of higher gas velocities, and thus the inter-particle interaction force play a comparatively important role in the gas-solid flow dynamics. The specific lower limit explored represents the lowest gas velocity at which, for the particular distributor explored in experiment, the presence of significant dead zones near the base of the system is avoided.

The time steps for the CFD-DEM simulations are determined by two important parameters, i.e., the Courant number (Co) and the Rayleigh time step (Δt_{max}).

Firstly, the Co is defined as (Courant, Friedrichs, & Lewy, 1928)

Table 4
Input parameters under different CG factors.

Case No.	λ (−)	N (Thousand)	$d_{p,max}$ (mm)	Mesh size (mm)
1	3	1197	1.5	3.13
2	4	505	2.0	3.13
3	8	63	4.0	4.27
4	12	19	6.0	6.71
5	15	10	7.5	7.83
6	18	6	9.0	9.40

$$\mathrm{Co} = \frac{|\mathbf{u}_g|\Delta t_{\mathrm{CFD}}}{\Delta L} \tag{1}$$

where Δt_{CFD} is the time step in the CFD solver. When the Co > 1, instabilities are amplified throughout the computational domain.

Secondly, according to Rayleigh theory (Hlosta et al., 2020), the maximum time step in the DEM simulation is estimated as

$$\Delta t_{max} = \frac{\pi R}{0.163\nu + 0.8766}\sqrt{\frac{\rho_p}{G}} \tag{2}$$

where G is the shear modulus, ν is the Poisson's ratio. A time step around 20%–80% Δt_{max} is generally considered suitable for the DEM simulations (Hlosta et al., 2020).

In order to achieve high numerical stability in the CFD-DEM simulation, $\Delta t_{CFD} = 10^{-4}$ s and $\Delta t_{DEM} = 10^{-6}$ s were set to ensure Co <0.05 and $\Delta t_{DEM} \approx 0.3\Delta t_{max}$.

As the "divided" void fraction model is applied in this study, the particle size in CFD-DEM simulations should be in the size range of a CFD cell (Kloss et al., 2012). For Cases 2–6, the CFD meshes were built with the cell size slightly greater than the maximum size of the particles after CG (see Table 4). In order to control the size of the mesh easily, the CFD mesh generator snappyHexMesh (https://www.openfoam.com/documentation/guides/latest/doc/) in OpenFOAM was applied. The mesh independence tests will be described in the following section.

4. Post-processing of the data from PEPT and CFD-DEM

4.1. Occupancy and solid velocity

Both PEPT measurements and the DEM solver used output data providing the instantaneous coordinate of the particle(s) at a series

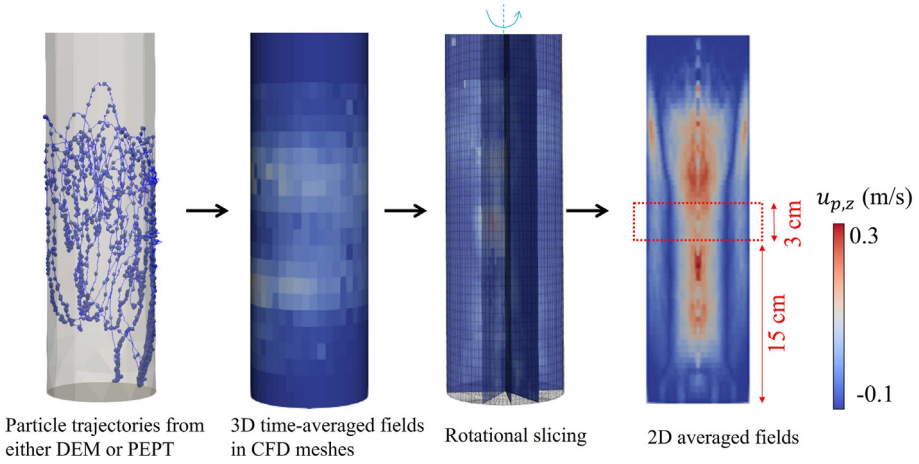

Fig. 4. Procedures for extracting the 2D averaged fields using the particle trajectories from either DEM or PEPT.

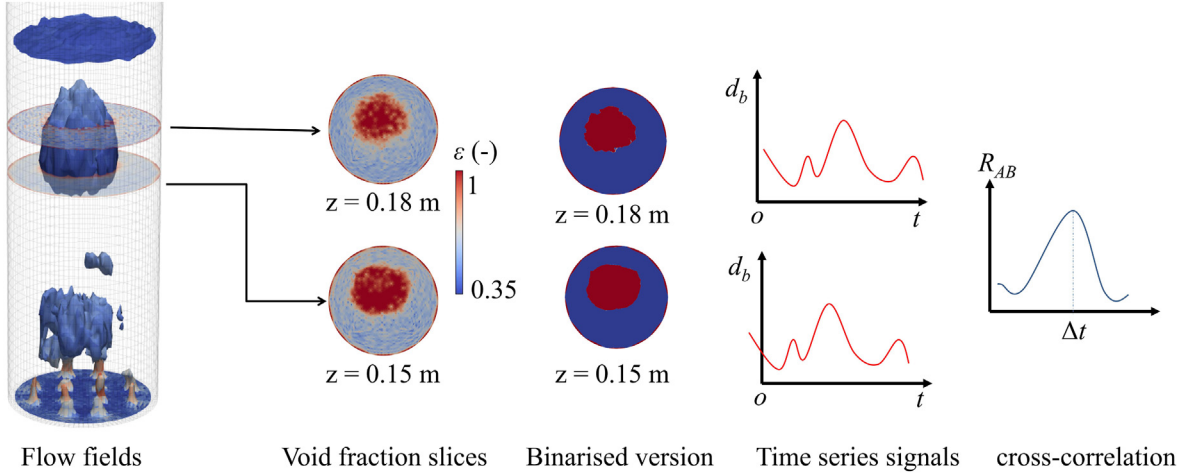

Fig. 5. Flow chart to determine the bubble diameter and bubble velocity using the CFD-DEM simulation results.

Table 5
Mesh size used in the tests.

	Fine	Medium	Coarse
Cell number (–)	113402	46975	5533
Cell side length (mm)	3.13	4.27	9.40

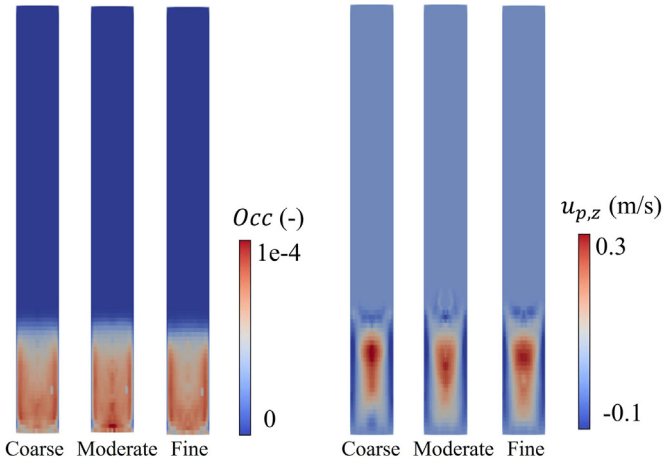

Fig. 6. particle occupancy and velocity distributions in simulations using different mesh densities.

of consecutive timesteps. Time-averaged process variables can be extracted by further evaluating these data in Eulerian grids in space. The fractional particle occupancy and the particle velocity are two variables of great interest for industrial applications, and can be extracted directly from both PEPT and CFD-DEM data. In order to compare the experimental and numerical results rigorously, the Lagrangian data from DEM and PEPT are post-processed using precisely the same procedure. An introduction to the approaches for extracting time-averaged Eulerian fields from the Lagrangian data can be found in (C. Windows-Yule, Gibson, et al., 2020), with a more detailed description provided in (K. Windows-Yule et al., 2022). To ensure a reliable and rigorous comparison between experiments and simulations, the trajectories of 3000 particles within the physical time of 10 s are randomly selected to generate the time-averaged fields, which is effectively equivalent to an 8-h PEPT experiment using a single tracer particle, thus more than ensuring good statistics. The CFD meshes are used as the background grid for the time-averaged fields extraction, and the Visualization Toolkit (VTK) (https://vtk.org/) was used in the post-processing.

Fig. 4 shows the procedures for extracting the 2D averaged fields using the particle trajectory from either DEM or PEPT. Using one slice per 1 degree rotation from the 3D field (either particle velocity or fractional occupancy), 360 slices were extracted and averaged. As particle flow near the air distributor cannot be precisely reproduced by the CFD-DEM simulations (the reason for this will be discussed in section 5.2), the occupancy and velocity curves in the following text are extracted from the area far from the air distributor (15–20 cm above, see the red box in Fig. 4) so as to allow meaningful comparison of experiment and simulation.

4.2. Bubble size and rising velocity

Bubbles are generated at the bottom of the fluidised bed and coalescence of bubbles occurs as they move upwards. The bubbles finally burst through the bed surface. Fig. 5 shows the flow chart to determine the bubble diameter and bubble rising velocity using the

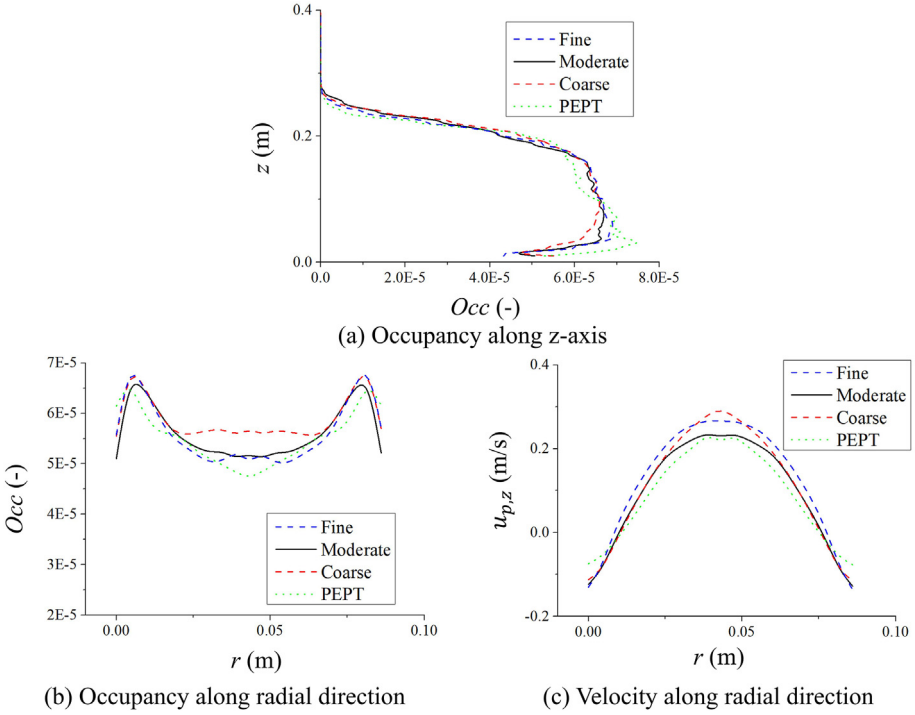

Fig. 7. particle occupancy and velocity distributions in simulations using different mesh densities.

Table 6
Root mean squared error (RMSE) in mesh grid independence test.

Variables	Fine	Medium	Coarse
$u_{p,z}$ (m/s)	0.0518	0.0277	0.03911
Occ_r (−)	5.73E-6	6.29E-6	8.35E-6
Occ_v (−)	3.98E-6	4.64E-6	5.52E-6

Table 7
Root Mean Square Error (RMSE) of variables in the first and second half of the data in the PEPT experiment.

Variables	2 u_{mf}	3 u_{mf}
$u_{p,z}$ (m/s)	0.010	0.021
Occ_r (−)	5.43e-6	5.05e-6
Occ_v (−)	5.1e-6	1.92e-6

CFD-DEM simulation results. The equivalent bubble diameter (d_b) is normally estimated based on its occupied 2D area (A_b) in plan view (Glicksman, Lord, & Sakagami, 1987; Sakai et al., 2010). The relationship between a given bubble's diameter and its occupied area can be taken as

$$d_b = \sqrt{\frac{4}{\pi} A_b} \tag{3}$$

For comparison with simulation results, the correlation proposed by Darton et al. (Darton, Rd, Jf, & D, 1977) will be used to calculate the theoretical bubble size:

$$d_b = 0.54\left(u_{fl} - u_{mf}\right)^{0.4}\left(h + 4\sqrt{A_0}\right)^{0.8} \Big/ g^{0.2} \tag{4}$$

where d_b is the diameter of the sphere having the same volume as the bubble, u_{fl} and u_{mf} are the superficial gas velocity and the minimum fluidization gas velocity, h is the height above the air distributor, A_0 is the area of the distributor plate per orifice (i.e. the area of the distributor plate divided by the number of orifices), and g is gravity acceleration.

In order to calculate the bubble velocity (u_b), the concept of cross-correlation coefficient is applied. Cross correlation methods were initially used in flow meters to determine the fluid velocity (Beck, 1981), and have been extended to determine the bubble velocity in a fluidised bed (Mao, Ye, Wang, & Yang, 2016). The idea of this method is calculating the flow velocity based on the transit time (Δt) of a tagging signal crossing two fixed positions along the flow. The tagging signal applied in this work is the time-series signals of bubble size. The cross-correlation (R_{AB}) of the signals (d_b^A and d_b^B) recorded from the positions A and B in the flow direction is calculated by (Mao et al., 2016)

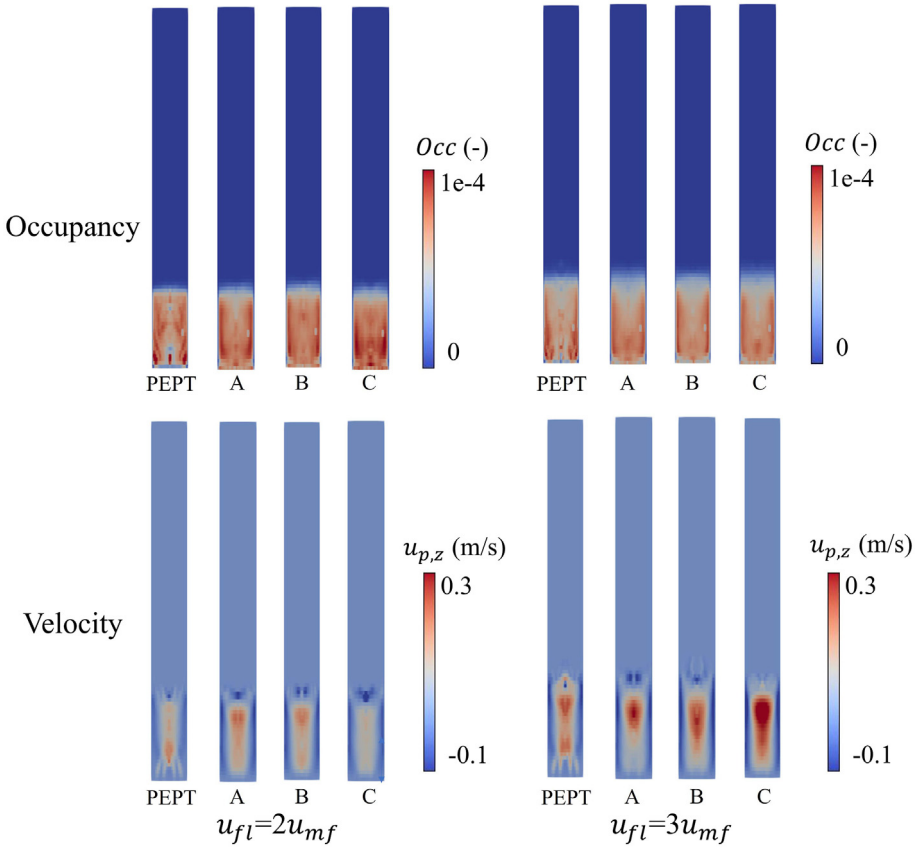

Fig. 8. particle occupancy and velocity distributions ($\lambda = 4$).

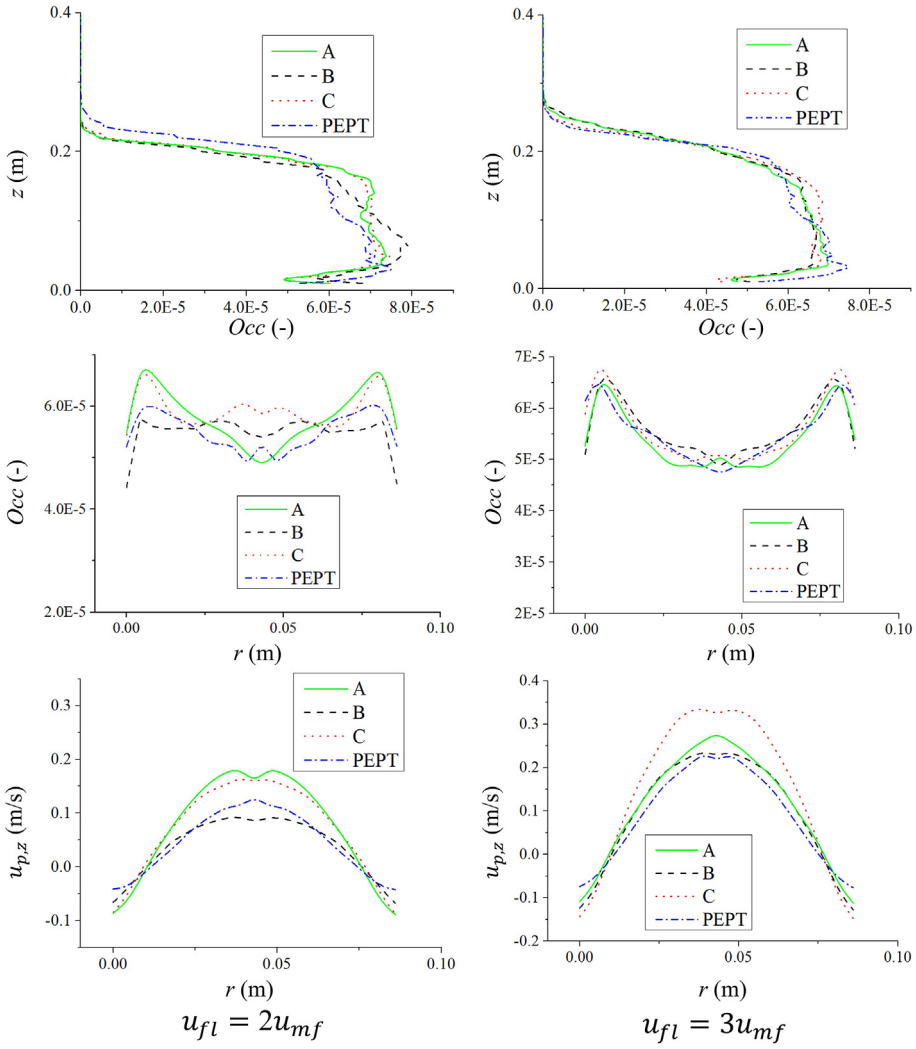

Fig. 9. particle occupancy and velocity profiles from PEPT and different CG CFD-DEM methods ($\lambda = 4$).

$$R_{AB}(j) = \frac{\sum_{i=1}^{N}\left(d_b^A(i) - \overline{d_b^A}\right)\left(d_b^B(i+j) - \overline{d_b^B}\right)}{N}, -N \Big/ 2 < j < N \Big/ 2 \tag{5}$$

where N is the length of the time-series bubble diameter signal, i is the index of the element of the signal, j is the delay frames of the two signals. The signals of d_b^B are periodically extended in the calculation as $i+j$ could be greater than N. Based on $R_{AB}(j)$, Δt is equal to the transit time (calculated by the delay frames) where R_{AB} achieves its maximum value.

5. Results and discussion

5.1. Mesh grid independence tests

A CG factor of 4 is selected to carry out mesh grid independence tests, as this value represents a moderate computational load yet can be run using meshes with a wide range of cell sizes. Table 5 shows the size and the number of the mesh used for the test cases. Fig. 6 shows the velocity and occupancy profiles under three sets of meshes. Based on the data in Figs. 6 and 7 compares averaged one-dimensional curves extracted from both CFD-DEM and PEPT data, and Table 6 shows the root mean squared error (RMSE) between the curves from CFD-DEM and PEPT. To facilitate comparison of data, and a quantification of the accuracy of the simulations, these values are compared to RMSE values calculated in each experiment using the first half and second half of the PEPT data, thus providing a measure of experimental error (as shown in Table 7). If the RMSE corresponding to the deviation of simulation

Table 8
Root Mean squared error (RMSE) between CFD-DEM and PEPT results in Cases 1 and 2.

Cases	Variables	CG methods		
		A	B	C
Case 1 ($\lambda = 4$, $u_{fl} = 2\ u_{mf}$)	$u_{p,z}$ (m/s)	0.073	0.017	0.073
	Occ_r (−)	4.16E-06	4.48E-06	5.82E-06
	Occ_v (−)	7.35E-06	7.82E-06	7.02E-06
Case 2 ($\lambda = 4$, $u_{fl} = 3\ u_{mf}$)	$u_{p,z}$ (m/s)	0.031	0.028	0.089
	Occ_r (−)	4.11E-06	6.09E-06	5.32E-06
	Occ_v (−)	4.00E-06	4.64E-06	4.60E-06

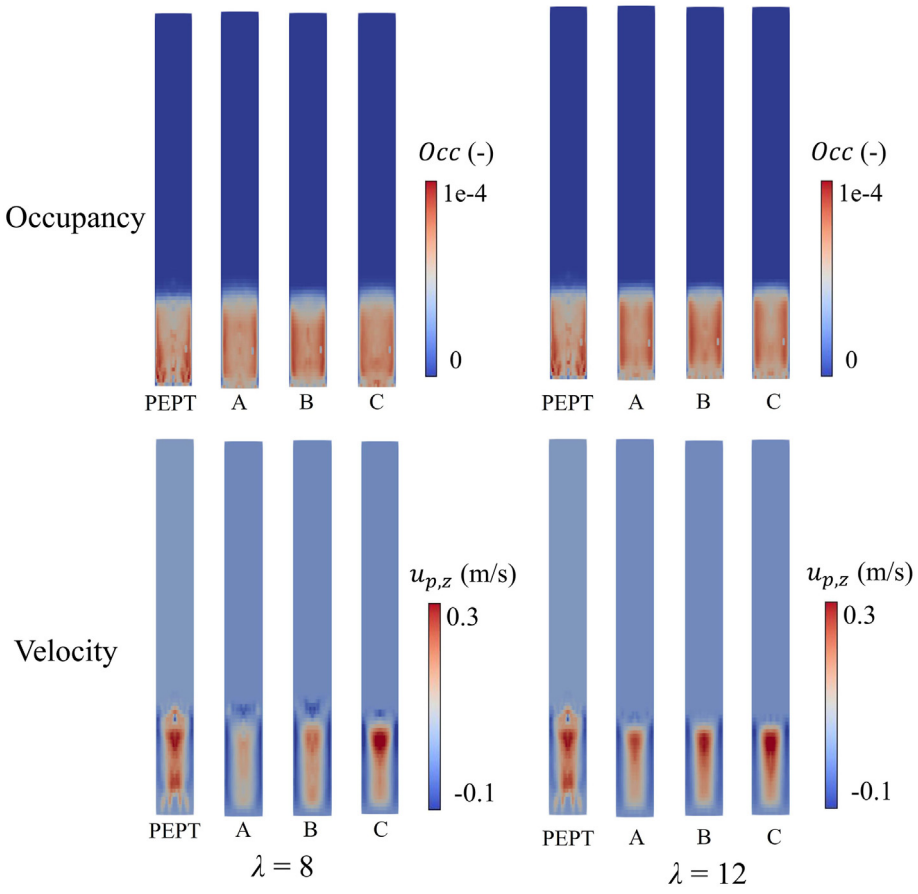

Fig. 10. particle occupancy and velocity profiles from PEPT and different CG CFDEM methods ($\lambda = 8$ and $\lambda = 12$).

from experiment is comparable to the RMSE quantifying experimental error, we can reasonably say that the simulation is accurate. Though some minor variations are observed between the different cases, reasonably close agreement is observed between the experiments and the simulations at different mesh sizes. The values of RMSE produced by CFD-DEM are all in the same order of magnitude both as one another and the values shown in Table 7, showing that mesh independence is fulfilled in these cases.

5.2. Comparison between CFD-DEM and PEPT results

Fig. 8 shows the particle occupancy and velocity profiles from PEPT and CFD-DEM CG methods A, B and C. Fig. 9 shows the time-average occupancy curve in radial and vertical directions, respectively; Table 8 shows the RMSE between the curves representing CFD-DEM and PEPT data. Overall, experiment and simulation results show good agreement, the curves have similar shapes, and RMSEs in Table 8 are in the same order of magnitude as the corresponding values shown in Table 7 – that is to say deviations from our experimental benchmarks are comparable in size to our experimental error margins, suggesting very strong agreement. The three CG methods show quite close trends in terms of the solid occupancy and velocity profiles, apart from method C which tends to overestimate the solid velocity, and yields comparatively greater RMSEs compared to methods A and B. It should be noted that some channels with high solid velocity exist at the bottom part of the fluidised bed in the experimental profiles, but they are not found in simulations. The difference is due to necessary simplifications made in the modelling of the air inlet in the CFD-DEM simulations. The diameter of the orifice in the experimental air distributor is only 1.2 mm (see Fig. 3), meaning that the local air velocity could reach 80–130 m/s, which results in some channels in local gas-solid flows at low heights within the system. However, the mesh size in CFD-DEM do not allow such a high resolution in the inlet velocity profile. We try to make the simulation input as close as possible to the real input parameters and the orifice diameter of 1 cm was set in the CFD-DEM simulation, but the channel cannot be reproduced. Though in a real (experimental) fluidised bed distributors of this size would likely cause maldistribution due to an uneven pressure drop (and thus gas velocity) across the plate (C. R. K. Windows-Yule, S. Gibson et al., 2020), in simulation a constant gas velocity can be directly imposed for all orifices, thus avoiding this issue. With this in mind, and considering also that the overall air mass flow rate is unchanged, and the orifices are uniformly distributed in a pattern equivalent to the experimental system (see Fig. 3), the size of orifice is expected to have negligible effects on the gas-solid flow in the upper part of the fluidised bed, where the solid occupancy and velocity profiles are quantitatively compared (see Fig. 4). The strong agreement seen between experiment and simulation in the preceding section suggests this to indeed be the case.

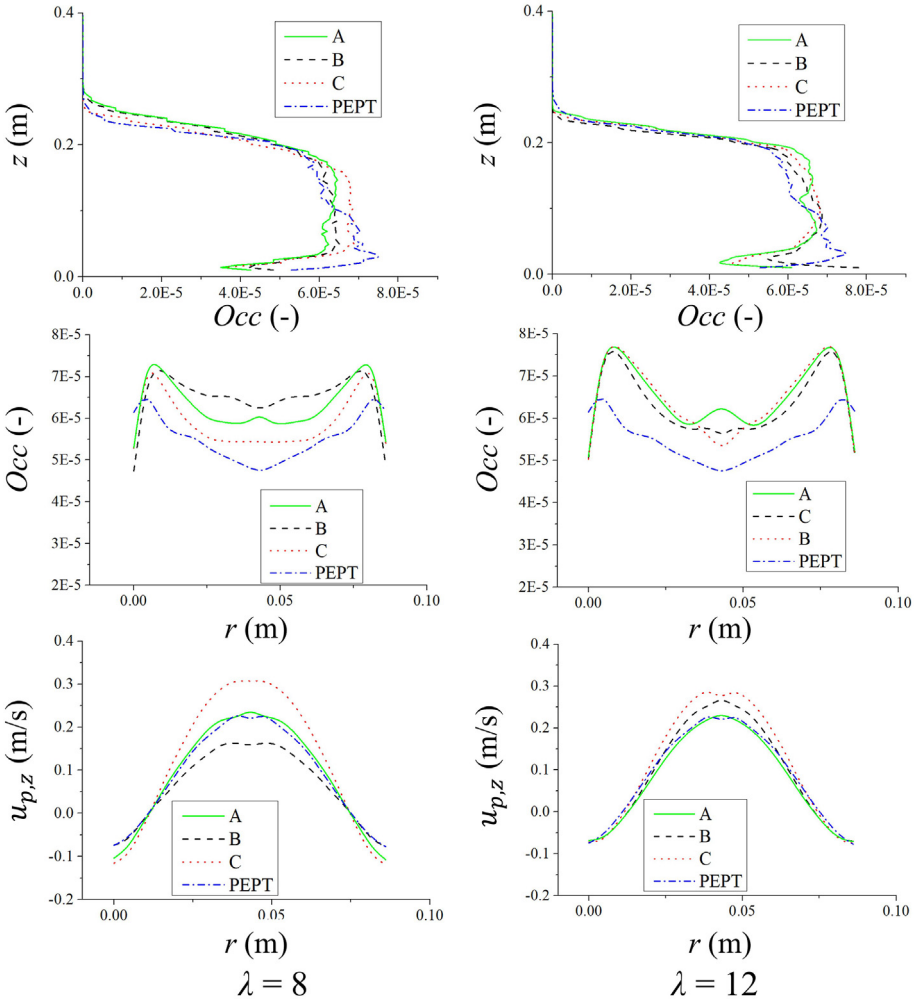

Fig. 11. particle occupancy and velocity profiles from PEPT and different CG CFDEM methods ($\lambda = 8$ and $\lambda = 12$).

Another issue that can be observed is that the occupancy was overestimated in the upper part of the fluidised bed but slightly underestimated in the bottom part. This is likely to be caused by the enlargement of the orifice size in the simulations, which may increase the size of bubbles at small heights, and thus in turn increase the transport of bed material from the lower to the upper region.

Fig. 10, Fig. 11 and Table 9 shows the simulation results under the Cases 3 and 4 (λ equals 8 and 12). The simulation accuracy deteriorates as the RMSEs increases beyond $\lambda = 4$, especially for the particle occupancy in the radial direction. Like the case of $\lambda = 4$, CG method C overestimates the solid velocity while methods A and B provide much closer results to the experimental case. However, no substantial differences were found in terms of the time-averaged occupancy profiles of the three CG methods.

In order to explore the effect of the CG factor on the simulation results, the curves from cases with different λ (with the same CG method A) are shown in Fig. 12; corresponding RMSE values are shown in Table 10. With increasing λ, that is, higher coarse-graining factors, the accuracy of the CFD-DEM simulations is generally worse, as the curves begin to lie further from the experimental data, and the RMSE correspondingly increases, especially for the radial velocity profiles under the $\lambda = 15$ and 18 cases. Although the RMSE values get lower as λ increases from 15 to 18, this does not indicate increasing accuracy, as the CG model of the CFD-DEM is no longer valid under such λ meaning that the value of RMSE is uninformative.

The sharp drop in accuracy observed for the $\lambda = 15$ and 18 cases could potentially be caused by two factors: either the CG factor is outside the range of its application in absolute terms, or the size ratio (θ) between the particles and the bed chamber is too large. To distinguish between these two possibilities, additional simulation cases using a 200 mm diameter fluidised bed were carried out for comparison. In this geometry, θ is only half of its equivalent value for the 94 mm cases at the same λ. As the particle number is very large for this case, only large λ values of 12, 15, 18, 20, 30 and 40

Table 9
Root mean squared error (RMSE) in cases with $\lambda = 8$ and $\lambda = 12$.

Cases	Variables	CG methods		
		A	B	C
Case 3 ($\lambda = 8$, $u_{fl} = 3\ u_{mf}$)	$u_{p,z}$ (m/s)	0.016	0.034	0.059
	Occ_r (−)	1.30E-05	1.59E-05	9.02E-06
	Occ_v (−)	8.06E-06	6.68E-06	6.12E-06
Case 4 ($\lambda = 12$, $u_{fl} = 3\ u_{mf}$)	$u_{p,z}$ (m/s)	0.014	0.021	0.038
	Occ_r (−)	1.56E-05	1.53E-05	1.35E-05
	Occ_v (−)	6.73E-06	6.11E-06	6.19E-06

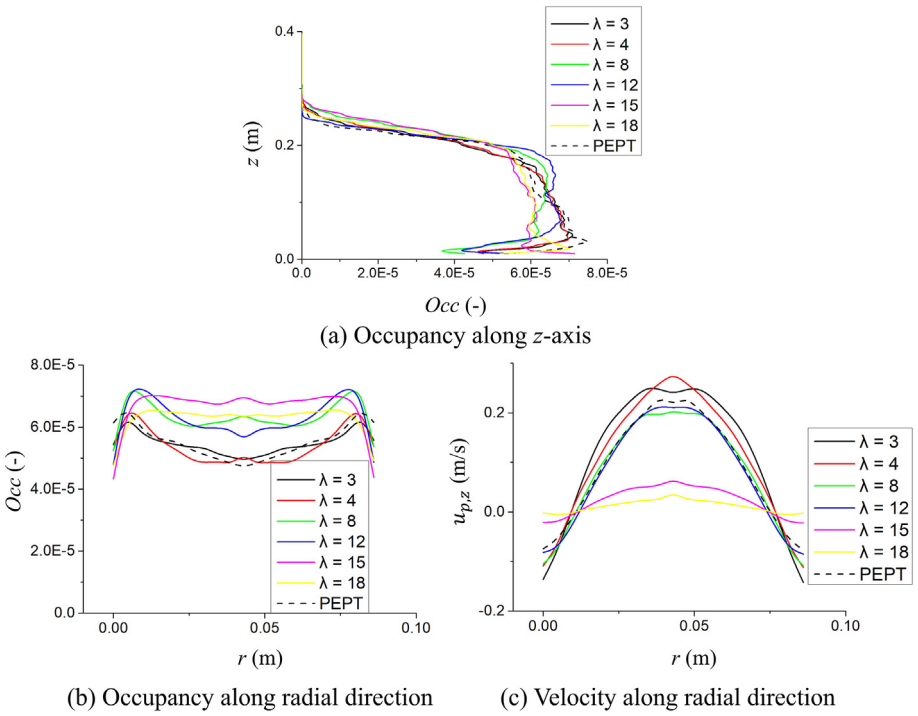

(a) Occupancy along z-axis

(b) Occupancy along radial direction

(c) Velocity along radial direction

Fig. 12. Comparison of experiment results with simulations at different λ.

were considered in the CFD-DEM simulation. The quantitative results from the additional simulations are shown in Fig. 13. Good agreements and no obvious difference are observed with the λ increased to 20, which shows that an upscaling factor of 15 is *not* an upper limit of the CG in absolute terms. When λ reaches 30, however, discrepancies appear in the occupancy and velocity curves, which indicates that the CG method is starting to fail. It should be noted that for fluidised beds with diameters of 94 mm and 200 mm, the simulations both start to fail when the value of θ approaches 20 (corresponding to $\lambda = 15$ and 30, respectively for the two cases). As such, our results suggest that it is the relative, as opposed to absolute, size of the particles that is the limiting factor in our present case. Accordingly, the size ratio should not exceed 20 for the bubbling bed system considered in this work.

5.3. Bubble size and rising velocity

The bubble size and rising velocity are indicators of the transient properties of the gas-solid flow compared to the time-averaged profiles shown in the sections above. The procedures to extract bubble size and velocity have been shown in section 4.2. Fig. 14 shows the changes in the instantaneous bubble diameter over time for two slices at $z = 0.15$ m and 0.18 m; the bubble size is calculated based on the maximum value at each cycle, and the transit time of the bubble motion between these two slices can be observed. Fig. 15 shows the correlation coefficient of the time-series bubble diameter signal; the transit time (Δt) corresponds to the maximum correlation coefficient and corresponds to the time for a bubble to travel from one slice to another, from which the characteristic bubble velocity can be calculated.

The bubble size and velocity achieved from different CG methods (A, B and C in Cases 2 and 3) are shown in Fig. 16. As PEPT cannot be used to (directly) image bubbles, we compare here instead to a widely-used predictive equation, namely the Darton equation (Darton et al., 1977). It is clear that methods A and B show very close values of bubble size to the value from the Darton equation, while method C is less accurate and always achieves the smallest bubble size. On the other hand, the bubble velocities are in the range 0.6–0.7 m/s and do not show clear trends between the three CG methods.

The bubble size and velocity at different λ are shown in Fig. 17, results of CG method A being used for each case. Again, CFD-DEM simulations are in close agreements with Darton's formula in terms of the bubble size, and no clear trend can be observed in the bubble velocity at different λ, though the case with $\lambda = 18$ achieved the highest bubble velocity. A certain decrease in the size of the bubbles occurs as λ increases to 12, and becomes obviously lower than the theoretical value, which means that the use of high coarse-grain degrees may underestimate the bubble size.

Table 10
Root mean squared error (RMSE) in Cases with different λ.

λ (−)	Variables used in the comparison		
	$u_{p,z}$ (m/s)	Occ_r (−)	Occ_v (−)
3	0.047	4.24E-06	3.66E-06
4	0.031	4.11E-06	4.00E-06
8	0.016	1.30E-05	8.06E-06
12	0.014	1.56E-05	6.73E-06
15	0.139	5.17E-05	6.17E-06
18	0.123	1.42E-05	4.82E-06

5.4. Discussion on the particle percolation throughout the fluidised bed

The particle percolation can be assessed by the segregation of the particles, which is an important consideration in many industrial processes (C. R. K. Windows-Yule, S. Gibson et al., 2020). In

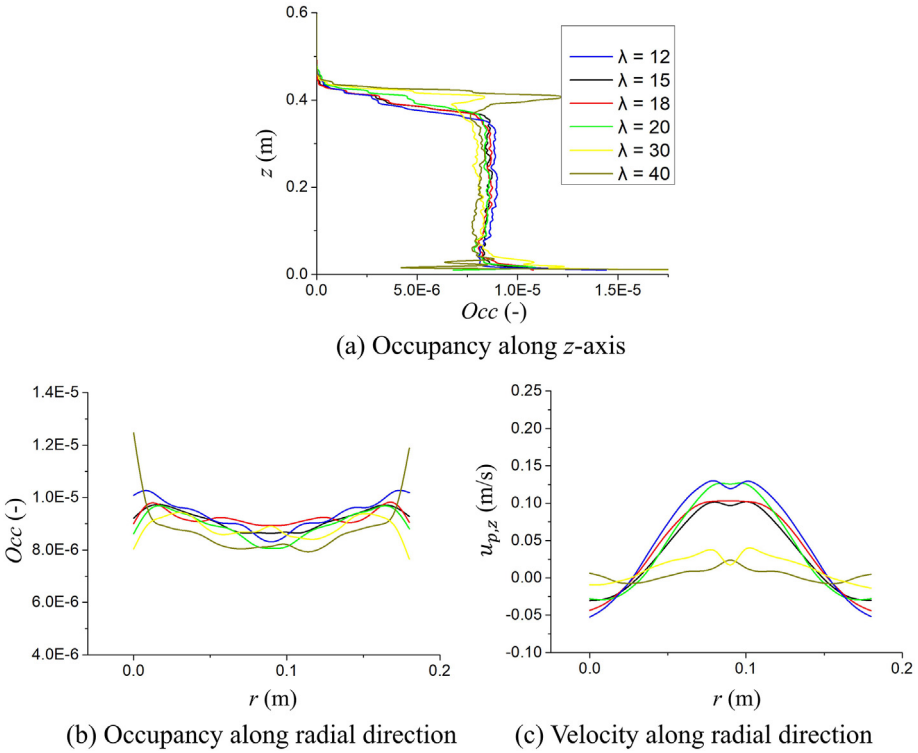

Fig. 13. Comparison of simulation results at different λ for the fluidised bed with the diameter of 200 mm.

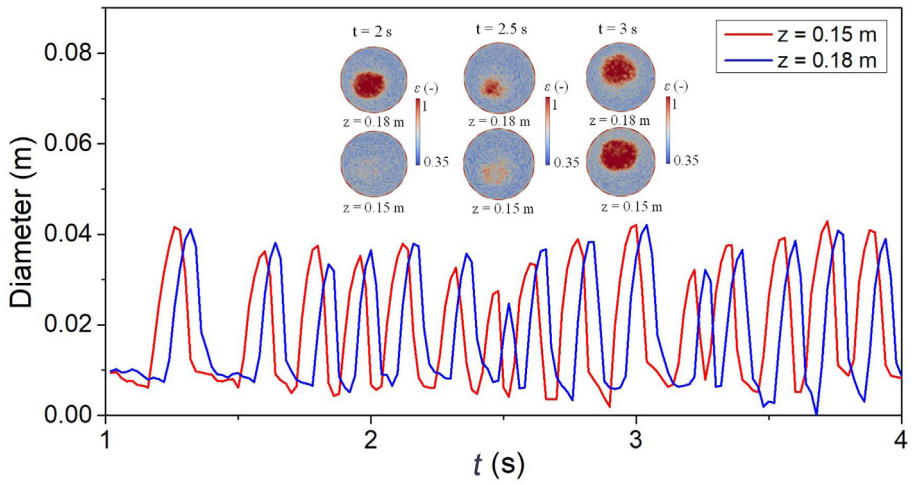

Fig. 14. Changes in the instantaneous bubble diameter over time for Case 3.

order to quantify the effect of the CG on the percolation/segregation of the particles, the averaged particle size along the z-axis within the last second (100 data frames in total) of the simulation are shown in Fig. 18. Simulations were performed for the cases $\lambda = 4$, 8 and 12; the blue line represents the average particle diameter at $t = 0$. For the lowest CG factor explored, the mean particle size remains approximately constant with height throughout the system, and aligns at all heights closely with the overall mean particle size, thus clearly demonstrating the absence of any meaningful segregation. This is not a surprising observation considering the fact that bubbling fluidised beds are well known to induce strong mixing between particles. This lack of segregation is similarly reflected in out PEPT data, where repeat measurements using tracers of different sizes yield near-identical occupancy profiles. A similar degree of consistency with height is observed for the $\lambda = 8$ case. For the $\lambda = 15$ case, considerably more fluctuation about the mean is observed. However, the lack of a clear trend (i.e. a monotonic variation in particle size with height as one would expect for percolation-based segregation (Rosato & Windows-Yule, 2020) suggests this fluctuation to be simply due to statistical noise as opposed to the presence of any physical segregation mechanism.

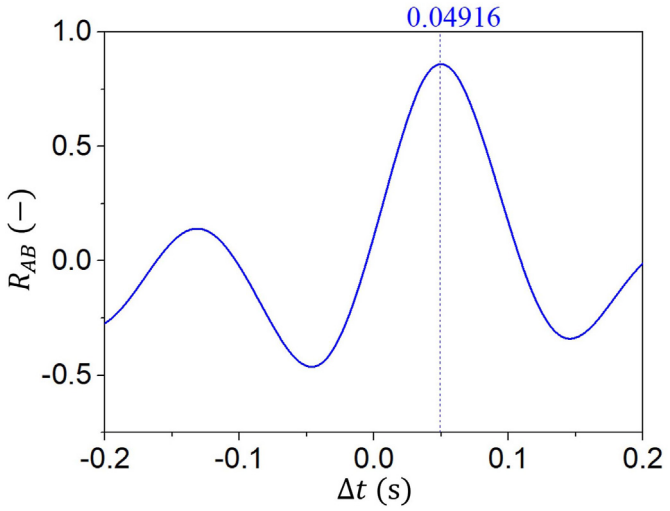

Fig. 15. Changes in the correlation coefficient of the time-series bubble diameter data (see Fig. 14) with the time offsets.

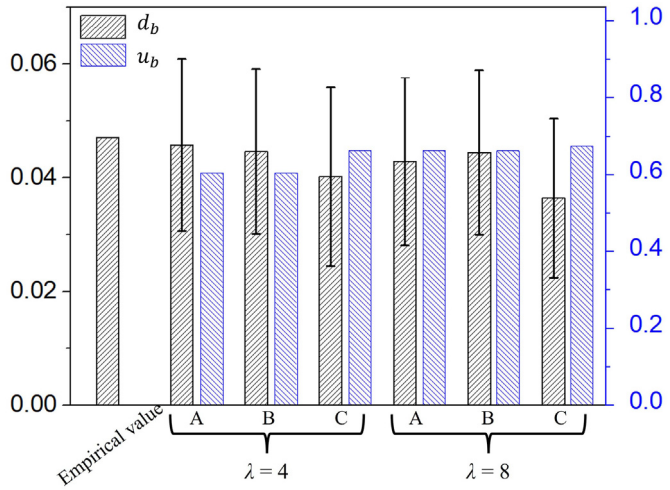

Fig. 16. Changes in the bubble size and rising velocity under different CG methods.

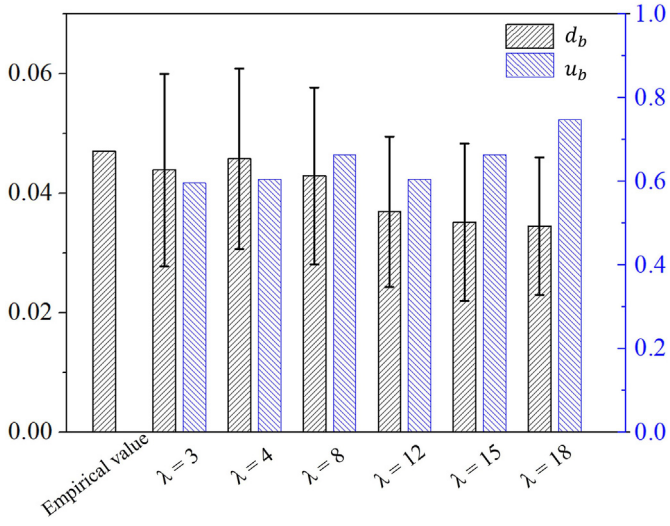

Fig. 17. Changes in the bubble size and velocity at different λ.

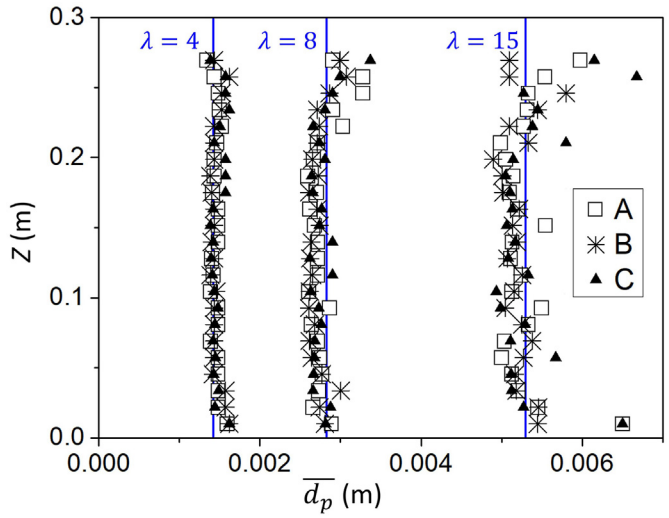

Fig. 18. Averaged particle size along z-axis extraction from the CFD-DEM simulations.

6. Conclusions

The performance of three different CFD-DEM coarse-graining methods under a wide range of coarse-graining factors has been evaluated based on the simulations of a simple, archetypal bubbling fluidised bed. High resolution experimental data from positron emission particle tracking (PEPT) measurements were used to validate the CFD-DEM simulations, and thus establish the abilities and limits of various commonly-used coarse-graining models. The main conclusions drawn are as follows.:

(1) Three typical coarse-graining methods were explored, and all three found to facilitate a reasonable degree of quantitative accuracy under suitable conditions, though the constant absolute overlap and constant relative overlap approaches to coarse-graining were in general shown to be more successful than the dimensionless number approach, in particular in predicting particle velocities.

(2) Our results do not demonstrate an upper limit for the absolute degree of coarse-graining which can be applied whilst still maintaining realistic bed behaviours, with scale-up factors >20 shown to be capable of producing meaningful results. This is a valuable result, as these CG factors would facilitate a reduction in particle number by a factor of more than 8000. However, agreement between simulation and experiment is shown to break down considerably when the *relative* size of the particles (compared to the system diameter) exceeds a ratio of $\sim 1:20$. Future work to further test the absolute limits of coarse-graining would be valuable.

(3) Except for the solid velocity profile, no significant improvements are observed through the use of complex CG models that account for the particle contact force. This can be explained by the fact that the gas-solid interaction force plays a dominate role in the particle flow, with the particle contact properties being less important, though nonetheless not irrelevant.

(4) The bubble size was underestimated using high degrees of coarse-graining, though values remain broadly consistent with theoretical predictions up to a CG factor of 18, the CG method derived from the dimensionless number showing obviously lower bubble sizes that the other two methods. On the other hand, the bubble velocities produced by different methods (and λ) did not show significant differences, though the CG methods accounting for the inter-particle contact

force have slightly better performance in prediction of the bubble size.

Although the above conclusions were drawn primarily for laboratory-scale bubbling fluidised beds, the applicability of simulations with relatively high CG factors has been demonstrated. Thus, it is expected that they can be extended to industrial-scale ones. While, based on our studies, we can be confident that the observations described above should hold for any bubbling fluidised bed with a gas flow rate greater than or equal to twice the minimum fluidization velocity, we cannot state with confidence whether all of our findings would hold true for lower flow velocities. Nonetheless, as at $2U_{mf}$ particle contacts can already be reasonably enduring, we are hopeful that our results will hold even for lower flow rates, so long as the bed is fully-fluidised, though this should still be explicitly tested.

Future work will need to explore the applicability of the CG method to other types of fluidised beds, such as the circulating fluidised bed and spouted bed. In the current paper we have established the limits on coarse graining in terms of mesoparticle diameter relative to system diameter; in future, it would be valuable to determine the *absolute* limits of the coarse-graining methods employed. Finally, in the present work the distribution of particle sizes explored was seemingly too narrow to allow the observation of any segregative behaviour. It would be interesting, in future, to explore a more strongly bi- or poly-disperse system so as to analyse the influence of coarse graining on a simulated system's segregative dynamics.

$$\frac{1}{g}\frac{\mathrm{d}\mathbf{u}_i}{\mathrm{d}t}=\underbrace{\sum_{j=1}^{N_{pp}}\left[\frac{F_{n,ij}}{m_i g}\left(\mathbf{n}+\frac{F_{t,ij}}{F_{n,ij}}\mathbf{t}\right)\right]}_{\text{Inter-particle contact}}+\underbrace{\frac{\mathbf{F}_{pf,i}}{m_i g}}_{\text{Particle-fluid interaction}}+\frac{\mathbf{g}}{g} \tag{A-3}$$

Declaration of competing interest

The authors declare that they have no known competing financial interests or personal relationships that could have appeared to influence the work reported in this paper.

Acknowledgments

This work was supported by the UK Engineering and Physical Sciences Research Council (EPSRC) grant EP/T034327/1 and the Royal Academy of Engineering grant IF\2021_89. The computations described in this paper were performed using the University of Birmingham's BEAR Cloud service, which provides flexible resource for intensive computational work to the University's research community. See http://www.birmingham.ac.uk/bear for more details.

Appendix A

The total packing volume of particles should be constant with different CG factors (λ), and the parameters of d_p, k_n, k_t, γ_n, γ_t etc. are adjusted to ensure the similar gas-solid flow behaviours. The acceleration due to gravity, g, is constant throughout. According to the constant packing volume of particles, the following equation is fulfilled:

$$\frac{4}{3}\pi d_{p,1}^3 N_1=\frac{4}{3}\pi d_{p,2}^3 N_2 \tag{A-1}$$

where N represents the number of particles, sub-indices 1 and 2 represent the variables of the original and CG system respectively. The CG particle number is given by

$$N_1=\lambda^3 N_2 \tag{A-2}$$

A.1 Contact interaction method

There are quite a few ways to derive the CG rules for the particle contact force (Bierwisch et al., 2009; Di Renzo et al., 2021; Mu et al., 2020; Nasato, Goniva, Pirker, & Kloss, 2015; Radl et al., 2011). We present it using a method that is easy to understand (Che, Wang, Xu, & Ge, 2022; Mu et al., 2020). In order to maintain similar particle hydrodynamic behaviour in the two systems, the ratio between the external forces and force of gravity on particles should be kept constant (Mu et al., 2020). Here the solid motion equation shown in Table 2 is divided by the particle gravity force $m_i g$ as

The magnitudes of the two labelled dimensionless groups, i.e., inter-particle contact and particle-fluid interaction on equation (A-3) should be kept constant under different λ.

(1) Inter-particle contact force

Two approaches, i.e., constant absolute overlap and constant relative overlap, were proposed for the inter-particle contact force CG. The former considers the same maximum overlap (δ_{ij}) between colliding particles, and the dissipated energy during collisions can be kept constant for impacts at the same velocity (Di Renzo et al., 2021). In contrast, the latter approach kept the relative overlap ($\frac{\delta_{ij}}{R_i}$) constant. Based on the linear spring-dashpot-slider formula shown in Table 2, the following equation is obtained:

$$\frac{F_{n,ij}}{m_i g}=\overbrace{\underbrace{\frac{k_n}{\rho_p V_{p,i} g}}_{C_1}\delta_{ij}-\underbrace{\frac{\gamma_n u_0}{\rho_p V_{p,i} g u_0}}_{C_2}\dot{\delta}_{ij}}^{\text{Constant absolute overlap}}=\overbrace{\underbrace{\frac{k_n R_i}{\rho_p V_{p,i} g}}_{C_3}\frac{\delta_{ij}}{R_i}-\underbrace{\frac{\gamma_n u_0}{\rho_p V_{p,i} g u_0}}_{C_4}\dot{\delta}_{ij}}^{\text{Constant relative overlap}} \tag{A-4}$$

C_1, C_2 and C_3, C_4 are identified as constant terms in the constant absolute overlap method and relative overlap method, respectively. According to the assumption in (Mu et al., 2020), we only consider the normal interparticle contact in the analysis and assume that the tangential contact parameters depend on the particle diameter and mass in the same way as the normal one.

(2) Particle-fluid interaction force

The fluid-particle interaction force can be expressed as (Zhou et al., 2010)

$$\mathbf{F}_{pf} = \mathbf{F}_d + \mathbf{F}_{\nabla p} + \mathbf{F}_{\nabla \bullet \tau} \approx \mathbf{F}_d/\varepsilon \tag{A-5}$$

The ratio between $\mathbf{F}_{pf}$ and gravity force for particle i can be expressed as

$$\frac{\mathbf{F}_{pf,i}}{m_i g} = \frac{\mathbf{F}_{d,i}/\varepsilon_i}{m_i g} = \begin{cases} \underbrace{\frac{\mu_f u_0}{g\rho_p R_i^2}}_{C_5} f_{erg}(\varepsilon_i, \mathrm{Re}_i) \frac{\mathbf{u}_f - \mathbf{u}_{p,i}}{u_0}, \varepsilon \le 0.8 \\ \frac{\mu_f u_0}{g\rho_p R_i^2} f_{w-y}(\varepsilon_i, \mathrm{Re}_i) \frac{\mathbf{u}_f - \mathbf{u}_{p,i}}{u_0}, \varepsilon > 0.8 \end{cases} \tag{A-6}$$

As ε_i and Re_i are invariant in the CG, the terms labelled C_5 should be identified as constant terms.

An analysis of the expressions of the terms (C_i) in the above groups, the following CG rules for the constant absolute overlap model are obtained:

$$\begin{aligned} &k_{n2} = \lambda k_{n,1}, \gamma_{n,2} = \lambda^2 \gamma_{n,1}, k_{t,2} = \lambda k_{t,1}, \\ &\gamma_{t,2} = \lambda^2 \gamma_{t,1}, \nu_{f,2} = \nu_{f,1}, p_{p,2} = \lambda^{-1} p_{p,1} \end{aligned} \tag{A-7}$$

Similarly, CG rules for the constant relative overlap model are listed as:

$$\begin{aligned} &k_{n2} = \lambda^2 \gamma_{n,1}, \gamma_{n,2} = \lambda^2 \gamma_{n,1}, k_{t,2} = \lambda k_{t,1}, \\ &\gamma_{t,2} = \lambda^2 \gamma_{t,1}, \nu_{f,2} = \nu_{f,1} p_{p,2} = \lambda^{-1} p_{p,1} \end{aligned} \tag{A-8}$$

A.2 Dimensionless number method

The idea of this CG method is keeping the dimensionless Archimedes number (Ar), Reynolds (Re) number, minimum fluidization velocity (u_{mf}) constant. Ar, Re and u_{mf} can be written as

$$\mathrm{Ar} = \frac{g d_p^3 (\rho_p - \rho_g)}{\rho_g \nu_g^2} \tag{A-9}$$

$$\mathrm{Re} = \frac{d_p (\boldsymbol{u}_g - \boldsymbol{u}_p)}{\nu_g} \tag{A-10}$$

$$u_{mf} = \frac{\mathrm{Re}_{mf} \nu_g}{d_p} \tag{A-11}$$

The following equation can be easily obtained by letting $u_{mf,1} = u_{mf,2}$ and $\mathrm{Re}_{mf,1} = \mathrm{Re}_{mf,2}$:

$$\nu_{g,2} = \lambda \nu_{g,1} \tag{A-12}$$

Similarly, by letting $\mathrm{Ar}_{mf,1} = \mathrm{Ar}_{mf,2}$, the CG rules for particle density can be written as

$$\rho_{p,2} = \frac{\rho_{g,2} (\rho_{p,1} - \rho_{g,1})}{\lambda \rho_{g,1}} + \rho_{g,2} \tag{A-13}$$

Following the CG rules by Che et al. (2022), the momentum source volume vector field in the CFD solver is forced to be adjusted to a value equal to that of the full-scale system.

References

Al-Shemmeri, M., Windows-Yule, K., Lopez-Quiroga, E., & Fryer, P. J. (2021). Coffee bean particle motion in a spouted bed measured using Positron Emission Particle Tracking (PEPT). *Journal of Food Engineering*, Article 110709.

Beck, M. S. (1981). Correlation in instruments: Cross correlation flowmeters. *Journal of Physics E: Scientific Instruments, 14*, 7–19.

Bierwisch, C., Kraft, T., Riedel, H., & Moseler, M. (2009). Three-dimensional discrete element models for the granular statics and dynamics of powders in cavity filling. *Journal of the Mechanics and Physics of Solids, 57*, 10–31.

Breuninger, P., Weis, D., Behrendt, I., Grohn, P., Krull, F., & Antonyuk, S. (2018). CFD–DEM simulation of fine particles in a spouted bed apparatus with a Wurster tube. *Particuology, 42*, 114–125.

Buist, K. A., van der Gaag, A. C., Deen, N. G., & Kuipers, J. A. M. (2014). Improved magnetic particle tracking technique in dense gas fluidized beds. *AIChE Journal, 60*, 3133–3142.

Che, H., Al-Shemmeri, M., Fryer, P. J., Lopez-Quiroga, E., Wheldon, T. K., & Windows-Yule, K. (2023). PEPT validated CFD-DEM model of aspherical particle motion in a spouted bed. *Chemical Engineering Journal, 453*, Article 139689.

Che, H. Q., Liu, D., Tian, W. B., Gao, S., Sun, J. T., & Xu, L. J. (2020). CFD-DEM study of gas-solid flow regimes in a Wurster type fluidized bed with experimental validation by electrical capacitance tomography. *Chemical Engineering Journal, 389*, Article 124280.

Che, H. Q., Wang, H. G., Xu, L. J., & Ge, R. H. (2022). Investigation of gas-solid heat and mass transfer in a Wurster coater using a scaled CFD-DEM model. *Powder Technology, 406*, Article 117598.

Che, H. Q., Ye, J. M., Tu, Q. Y., Yang, W. Q., & Wang, H. G. (2018). Investigation of coating process in Wurster fluidised bed using electrical capacitance tomography. *Chemical Engineering Research and Design, 132*, 1180–1192.

Courant, R., Friedrichs, K., & Lewy, H. (1928). Über die partiellen Differenzengleichungen der mathematischen Physik. *Mathematische Annalen, 100*, 32–74.

Cundall, P. A., & Strack. (1979). A Discrete numerical model for granular assemblies. *International Journal of Rock Mechanics and Mining Sciences & Geomechanics Abstracts, 29*, 47–65.

Darton, R., Rd, L., Jf, D., & D, H. (1977). Bubble growth due to coalescence in fluidized beds. *Transactions of the Institution of Chemical Engineers, 55*, 274–280.

Di Renzo, A., & Di Maio, F. P. (2004). Comparison of contact-force models for the simulation of collisions in DEM-based granular flow codes. *Chemical Engineering Science, 59*, 525–541.

Di Renzo, A., Napolitano, E. S., & Di Maio, F. P. (2021). Coarse-grain dem modelling in fluidized bed simulation: A review. *Processes, 9*, 279.

Ergun, S. (1952). Fluid flow through packed columns. *Chemical Engineering Progress, 48*, 89–94.

Glicksman, L. R., Lord, W. K., & Sakagami, M. (1987). Bubble properties in large-particle fluidized beds. *Chemical Engineering Science, 42*, 479–491.

Goniva, C., Kloss, C., Hager, A., & Pirker, S. (2010). An open source CFD-DEM perspective. In *Proceedings of OpenFOAM workshop, Göteborg* (pp. 22–24).

Grohn, P., Oesau, T., Heinrich, S., & Antonyuk, S. (2022). Investigation of the influence of wetting on the particle dynamics in a fluidized bed rotor granulator by MPT measurements and CFD-DEM simulations. *Powder Technology, 408*, Article 117736.

Gryczka, O., Heinrich, S., Miteva, V., Deen, N. G., Kuipers, J. A. M., Jacob, M., et al. (2008). Characterization of the pneumatic behavior of a novel spouted bed apparatus with two adjustable gas inlets. *Chemical Engineering Science, 63*, 791–814.

Hagemeier, T., Roloff, C., Bück, A., & Tsotsas, E. (2015). Estimation of particle dynamics in 2-D fluidized beds using particle tracking velocimetry. *Particuology, 22*, 39–51.
Heinrich, S., Dosta, M., & Antonyuk, S. (2015). Multiscale aalysis of a coating process in a Wurster fluidized bed apparatus. In *Advances in chemical engineering, 46* pp. 83–135). Academic Press.
Hlosta, J., Jezerská, L., Rozbroj, J., Žurovec, D., Nečas, J., & Zegzulka, J. (2020). DEM investigation of the influence of particulate properties and operating conditions on the mixing process in rotary drums: Part 1—determination of the DEM parameters and calibration process. *Processes, 8*, 222.
Hofbauer, H., & Materazzi, M. (2019). 7 - waste gasification processes for SNG production. In M. Materazzi, & P. U. Foscolo (Eds.), *Substitute natural gas from waste* (pp. 105–160). Academic Press.
Hoomans, B. P. B., Kuipers, J. A. M., Mohd Salleh, M. A., Stein, M., & Seville, J. P. K. (2001). Experimental validation of granular dynamics simulations of gas-fluidised beds with homogenous in-flow conditions using Positron Emission Particle Tracking. *Powder Technology, 116*, 166–177.
Iannello, S., Foscolo, P. U., & Materazzi, M. (2021). Investigation of single particle devolatilization in fluidized bed reactors by X-ray imaging techniques. *Chemical Engineering Journal*, Article 133807.
Julián, I., Gallucci, F., van Sint Annaland, M., Herguido, J., & Menéndez, M. (2012). Coupled PIV/DIA for fluid dynamics studies on a two-section two-zone fluidized bed reactor. *Chemical Engineering Journal, 207*, 122–132.
Kloss, C., Goniva, C., Hager, A., Amberger, S., & Pirker, S. (2012). Models, algorithms and validation for opensource DEM and CFD-DEM. *Progress in Computational Fluid Dynamics, an International Journal, 12*, 140–152.
Laverman, J. A., Fan, X., Ingram, A., Annaland, M.v. S., Parker, D. J., Seville, J. P. K., et al. (2012). Experimental study on the influence of bed material on the scaling of solids circulation patterns in 3D bubbling gas–solid fluidized beds of glass and polyethylene using positron emission particle tracking. *Powder Technology, 224*, 297–305.
Link, J. M., Cuypers, L. A., Deen, N. G., & Kuipers, J. A. M. (2005). Flow regimes in a spout–fluid bed: A combined experimental and simulation study. *Chemical Engineering Science, 60*, 3425–3442.
Link, J. M., Godlieb, W., Tripp, P., Deen, N. G., Heinrich, S., Kuipers, J. A. M., et al. (2009). Comparison of fibre optical measurements and discrete element simulations for the study of granulation in a spout fluidized bed. *Powder Technology, 189*, 202–217.
Liu, Z., Suda, T., Tsuji, T., & Tanaka, T. (2013). Use of similarities in CFD-DEM simulation of fluidized bed. In *The 14th international conference on fluidization. The Netherlands*.
Lu, L., Xu, Y., Li, T., & Benyahia, S. (2018). Assessment of different coarse graining strategies to simulate polydisperse gas-solids flow. *Chemical Engineering Science, 179*, 53–63.
Mao, M., Ye, J., Wang, H., & Yang, W. (2016). Investigation of gas–solids flow in a circulating fluidized bed using 3D electrical capacitance tomography. *Measurement Science and Technology, 27*, Article 095401.
Mohs, G., Gryczka, O., Heinrich, S., & Mörl, L. (2009). Magnetic monitoring of a single particle in a prismatic spouted bed. *Chemical Engineering Science, 64*, 4811–4825.
Moliner, C., Marchelli, F., Spanachi, N., Martinez-Felipe, A., Bosio, B., & Arato, E. (2019). CFD simulation of a spouted bed: Comparison between the discrete element method (DEM) and the two fluid model (TFM). *Chemical Engineering Journal, 377*, Article 120466.
Mori, Y., Wu, C.-Y., & Sakai, M. (2019). Validation study on a scaling law model of the DEM in industrial gas-solid flows. *Powder Technology, 343*, 101–112.
Mu, L., Buist, K., Kuipers, J., & Deen, N. (2020). Scaling method of CFD-DEM simulations for gas-solid flows in risers. *Chemical Engineering Science: X, 6*, Article 100054.
Nasato, D. S., Goniva, C., Pirker, S., & Kloss, C. (2015). Coarse graining for large-scale DEM simulations of particle flow—an investigation on contact and cohesion models. *Procedia Engineering, 102*, 1484–1490.
Neuwirth, J., Antonyuk, S., Heinrich, S., & Jacob, M. (2013). CFD–DEM study and direct measurement of the granular flow in a rotor granulator. *Chemical Engineering Science, 86*, 151–163.
Nicuşan, A., & Windows-Yule, C. (2020). Positron emission particle tracking using machine learning. *Review of Scientific Instruments, 91*, Article 013329.
Oesau, T., Grohn, P., Pietsch-Braune, S., Antonyuk, S., & Heinrich, S. (2022). Novel approach for measurement of restitution coefficient by magnetic particle tracking. *Advanced Powder Technology, 33*, Article 103362.
van Ommen, J. R., Sasic, S., van der Schaaf, J., Gheorghiu, S., Johnsson, F., & Coppens, M.-O. (2011). Time-series analysis of pressure fluctuations in gas–solid fluidized beds – a review. *International Journal of Multiphase Flow, 37*, 403–428.
Parker, D., Forster, R., Fowles, P., & Takhar, P. (2002). Positron emission particle tracking using the new Birmingham positron camera. *Nuclear Instruments and Methods in Physics Research Section A: Accelerators, Spectrometers, Detectors and Associated Equipment, 477*, 540–545.
Radl, S., Radeke, C., Khinast, J. G., & Sundaresan, S. (2011). Parcel-based approach for the simulation of gas-particle flows. In *8th international conference on CFD in oil & gas, metallurgical and process industries, trondheim, 23* pp. 1084–1098).
Rosato, A. D., & Windows-Yule, C. (2020). *Segregation in vibrated granular systems*. Academic Press.
Sakai, M., Abe, M., Shigeto, Y., Mizutani, S., Takahashi, H., Viré, A., et al. (2014). Verification and validation of a coarse grain model of the DEM in a bubbling fluidized bed. *Chemical Engineering Journal, 244*, 33–43.
Sakai, M., & Koshizuka, S. (2009). Large-scale discrete element modeling in pneumatic conveying. *Chemical Engineering Science, 64*, 533–539.
Sakai, M., Yamada, Y., Shigeto, Y., Shibata, K., Kawasaki, V. M., & Koshizuka, S. (2010). Large-scale discrete element modeling in a fluidized bed. *International Journal for Numerical Methods in Fluids, 64*, 1319–1335.
Seiler, C., Fryer, P., & Seville, J. (2008). Statistical modelling of the spouted bed coating process using positron emission particle tracking (PEPT) data. *Canadian Journal of Chemical Engineering, 86*, 571–581.
da Silva, C. A. M., Butzge, J. J., Nitz, M., & Taranto, O. P. (2014). Monitoring and control of coating and granulation processes in fluidized beds–A review. *Advanced Powder Technology, 25*, 195–210.
Stein, M., Ding, Y. L., Seville, J. P. K., & Parker, D. J. (2000). Solids motion in bubbling gas fluidised beds. *Chemical Engineering Science, 55*, 5291–5300.
Stein, M., Martin, T. W., Seville, J. P. K., McNeil, P. A., & Parker, D. J. (1997). Chapter 10 - positron emission particle tracking: Particle velocities in gas fluidised beds, mixers and other applications. In J. Chaouki, F. Larachi, & M. P. Duduković (Eds.), *Non-invasive monitoring of multiphase flows* (pp. 309–333). Amsterdam: Elsevier Science B.V.
Takabatake, K., Mori, Y., Khinast, J. G., & Sakai, M. (2018). Numerical investigation of a coarse-grain discrete element method in solid mixing in a spouted bed. *Chemical Engineering Journal, 346*, 416–426.
Tebianian, S., Dubrawski, K., Ellis, N., Cocco, R. A., Hays, R., Reddy Karri, S. B., et al. (2015). Investigation of particle velocity in FCC gas-fluidized beds based on different measurement techniques. *Chemical Engineering Science, 127*, 310–322.
Toschkoff, G., & Khinast, J. G. (2013). Mathematical modeling of the coating process. *International Journal of Pharmacy, 457*, 407–422.
Van de Velden, M., Baeyens, J., Seville, J. P. K., & Fan, X. (2008). The solids flow in the riser of a circulating fluidised bed (CFB) viewed by positron emission particle tracking (PEPT). *Powder Technology, 183*, 290–296.
Wang, H., & Yang, W. (2020). Application of electrical capacitance tomography in pharmaceutical fluidised beds–A review. *Chemical Engineering Science*, Article 116236.
Weller, H. G., Tabor, G., Jasak, H., & Fureby, C. (1998). A tensorial approach to computational continuum mechanics using object-oriented techniques. *Computers in Physics, 12*, 620–631.
Wen, C. Y., & Yu, Y. H. (1966). Mechanics of fluidization. *Chem.engng Prog.symp.ser, 62*, 100–111.
Werther, J., Hartge, E.-U., & Heinrich, S. (2014). Fluidized-bed reactors - status and some development perspectives. *Chemie Ingenieur Technik, 86*, 2022–2038.
Westerweel, J., Elsinga, G. E., & Adrian, R. J. (2013). Particle image velocimetry for complex and turbulent flows. *Annual Review of Fluid Mechanics, 45*, 369–396.
Wildman, R., Huntley, J., Hansen, J.-P., Parker, D., & Allen, D. (2000). Single-particle motion in three-dimensional vibrofluidized granular beds. *Physical Review E, 62*, 3826.
Windows-Yule, C. R. K., Gibson, S., Werner, D., Parker, D. J., Kokalova, T. Z., & Seville, J. P. K. (2020). Effect of distributor design on particle distribution in a binary fluidised bed. *Powder Technology, 367*, 1–9.
Windows-Yule, C. R., Herald, M., Nicusan, L., Wiggins, C., Pratx, G., Manger, S., et al. (2021). Recent advances in positron emission particle tracking: A comparative review. *Reports on Progress in Physics*.
Windows-Yule, C. R. K., Moore, A., Wellard, C., Werner, D., Parker, D. J., & Seville, J. P. K. (2020). Particle distributions in binary gas-fluidised beds: Shape matters – but not much. *Chemical Engineering Science, 216*, Article 115440.
Windows-Yule, K., Nicuşan, L., Herald, M. T., Manger, S., & Parker, D. (2022). *Positron emission particle tracking; A comprehensive guide*.
Windows-Yule, C., Seville, J., Ingram, A., & Parker, D. (2020). Positron emission particle tracking of granular flows. *Annual review of chemical and biomolecular engineering, 11*, 367–396.
Wong, Y. S., & Seville, J. P. K. (2006). Single-particle motion and heat transfer in fluidized beds. *AIChE Journal, 52*, 4099–4109.
Xu, Y., Li, T., Lu, L., Gao, X., Tebianian, S., Grace, J. R., et al. (2020). Development and confirmation of a simple procedure to measure solids distribution in fluidized beds using tracer particles. *Chemical Engineering Science, 217*, Article 115501.
Zhou, Z. Y., Kuang, S. B., Chu, K. W., & Yu, A. B. (2010). Discrete particle simulation of particle–fluid flow: Model formulations and their applicability. *Journal of Fluid Mechanics, 661*, 482–510.
Zhu, H. P., Zhou, Z. Y., Yang, R. Y., & Yu, A. B. (2007). Discrete particle simulation of particulate systems: Theoretical developments. *Chemical Engineering Science, 62*, 3378–3396.
Zhu, H. P., Zhou, Z. Y., Yang, R. Y., & Yu, A. B. (2008). Discrete particle simulation of particulate systems: A review of major applications and findings. *Chemical Engineering Science, 63*, 5728–5770.